https://doi.org/10.5194/nhess-2022-253
Preprint. Discussion started: 9 November 2022

Natural Hazards and Earth System Sciences
Discussions

Assessing Typhoon Soulik-induced morphodynamics over the Mokpo coast region in South Korea based on a geospatial approach

Sang-Guk Yum[1], Moon-Soo Song[2], Manik Das Adhikari[3*]

[1] Department of Civil Engineering, Gangneung-Wonju National University, Gangneung, Gangwon-do 25457, South Korea; skyeom0401@gwnu.ac.kr
[2] Interdisciplinary Program in Crisis, Disaster and Risk Management, Sungkyunkwan University, Suwon, Gyeonggi-do 2066, South Korea; sms0722@daum.net
[3] Department of Civil Engineering, Gangneung-Wonju National University, Gangneung, Gangwon-do 25457, South Korea; rsgis.manik@gmail.com

Correspondence to: Manik Das Adhikari (rsgis.manik@gmail.com)

Abstract

The inner shelf and coastal region of the Yellow Sea along the Korean peninsula are frequently impacted by Typhoons. The Mokpo coastal region in South Korea has been significantly affected by typhoon Soulik in 2018, the deadliest typhoon strike to the southwestern coast, since Maemi in 2003. Typhoon Soulik overran the region, causing extensive damage to the coast, shoreline, vegetation, and coastal geomorphology. Therefore, it is important to investigate its impact on the coastal ecology, landform, erosion/accretion, suspended sediment concentration (SSC) and associated coastal changes along the Mokpo region.

In this study, net shoreline movement (NSM), Normalized Difference Vegetation Index (NDVI)), coastal landform change model, Normalized Difference Suspended Sediment Index (NDSSI), and SSC-reflectance relation have been used to analyze the coastal morphodynamics over the typhoon periods. We used pre-and post-typhoon Sentinel-2B MSI images for mapping and monitoring the typhoon effect. The findings highlighted the significant impacts of typhoons on coastal dynamics, wetland vegetation and sediment resuspension along the Mokpo coast. It has been observed that typhoon-induced SSC influences shoreline and coastal morphology. The outcome of this research may provide databases to manage coastal environments and a long-term plan to restore valuable coastal habitats. In addition, the findings may be useful for post-typhoon emergency response, coastal planners, and administrators involved in the long-term development of human life.

Keywords: Typhoon Soulik, Coastal changes, NDVI, Suspended sediment movement, Shoreline change, Mokpo Coast.

https://doi.org/10.5194/nhess-2022-253
Preprint. Discussion started: 9 November 2022

1. Introduction

Typhoons are one of the most destructive natural calamities. Strong winds that accompany typhoons during landfall damage the environment, coastline, wildlife, people, and public and private properties in coastal and inland areas (Shamsuzzoha et al., 2021; Xu et al., 2021; Mishra et al., 2021a; Nandi et al., 2020; Sadik et al., 2020; Sahoo and Bhaskaran, 2018; Hoque et al., 2016). Many coastal and near-coastal countries are plagued by typhoon-induced storms, flooding, deforestation, and increased soil salinity (Rodgers et al., 2009). Typhoons (tropical cyclones) have caused 1,942 disasters in the past 50 years, resulting in 779,324 fatalities and USD 1,407.6 billion in economic losses worldwide (WMO, 2020), demonstrating their effects on both the global and regional economies (Bhuiyan and Dutta, 2012; Mallick et al., 2017). The effects of typhoons include saltwater intrusion, soil fertility depletion, reduced agricultural productivity, life losses, coastline erosion, vegetation damage, and massive economic disasters (Mishra et al., 2021b).

According to instrumental data collected since 1904, typhoon intensity on the Korean peninsula has grown during the previous 100 years (Yu et al., 2018; Cha et al., 2021). A total of 188 typhoons, about three annually, have affected the coastal region from 1959 to 2018 (KMA, 2018). Among past Typhoons, RUSA (2002), MAEMI (2003), NARI (2007) and SOULIK (2018) had heavily affected the southwestern coast, causing extensive damage to lives and properties (KMA, 2011; 2018). Furthermore, people living in these regions have faced serious coastal floods caused by these events for more than a half-century (Moon et al., 2003). Mokpo coastal region located in the southwest coast of South Korea has been hit by 58 typhoons since 1980, with most occurring in the July to October period (Kang et al., 2020; Lee et al., 2022). The rapid growth of coastal economies and populations in recent years has made these areas more susceptible to typhoon disasters. The increasing frequency of typhoons on the southwestern coasts is a significant issue for disaster management.

Several studies have been carried out in South Asia using various techniques to map the hazard, vulnerability, risk and effects of typhoon disasters (Halder and Bandyopadhyay, 2022; Wang et al., 2021; Shamsuzzoha et al., 2021; Kumar et al., 2021; Sadik et al., 2020; Konda et al., 2018; Parida et al., 2018; Zhang et al., 2013; Yin et al., 2013; Li and Li., 2013; Rodgers et al., 2009). Remote sensing and geospatial technology played a crucial role in monitoring a variety of natural disasters (Wang and Xu, 2018; Mishra et al., 2021b; Charrua et al., 2020). The majority of studies on typhoon-induced coastal dynamics rely on passive optical remote sensing and identify natural disaster damage using changes in landuse data, vegetation indices, and geospatial techniques (Mishra et al., 2021a; Xu et al., 2021; Nandi et al., 2020). The post-typhoon damage assessment research in South Korea mostly focused on property loss, economic losses, and casualties (Yum et al., 2021; Kim et al., 2021; Hwang et al., 2020). However, the coastal morphodynamics along the Mokpo coast over the typhoon period have not been investigated in detail. Thus, this study's primary focus is to determine the effects of typhoon Soulik on coastal ecology, landforms, erosion/accretion, suspended sediment movement and associated coastal changes along the Mokpo coast.

To map the extent of vegetation destruction and details on the degree of damage after the typhoon, the normalized difference vegetation index (NDVI) and changes in NDVI (ΔNDVI) have been utilized (Wang et al., 2010; Datta & Deb, 2012; Zhang et al., 2013; Kumar et al., 2021; Xu et al., 2021). Vegetation damage can be seen by the negative change in NDVI values between the post-and pre-typhoon period (Mishra et al., 2021a; Hu & Smith, 2018). The coastline movement over the typhoon periods has been analyzed using the Digital Shoreline Analysis System (DSAS) program (Tsai, 2022; Adhikari et al., 2021; Bishop-Taylor et al., 2021; Santos et al., 2021). In order to monitor and protect coastal habitats, we need to understand the distribution and movement of SSC between rivers and coastal waters. Thus, the Normalized Difference Suspended Sediment Index (NDSSI) (Kavan et al., 2022; Shahzad et al., 2018; Hossain et al., 2010) and the SSC-reflectance algorithm developed by Choi et al. (2014) for the Mokpo coastal region have been used to monitor SSC distribution. Furthermore, to understand the morphodynamics of the coastal landform due to the typhoon, a GSI-based coastal change model has been developed. Four coastal landform classes, i.e., tidally influence land (wetland land, wetland vegetation), non-tidally influence land (land and water) have been used for the coastal morphodynamic analysis (Maiti and Bhattacharya, 2011). The change detection technique has been employed to quantify the pre and post-typhoon coastal changes. This approach focuses on details of morphological changes within the coast and highlights the minor changes caused by the typhoon.

This study uses Sentinel-2 MSI images as a primary data source to examine the morphodynamics and effects of Typhoon Soulik on coastal ecology. Accordingly, the objectives of this study are to (i) quantify and mapping of coastal landform dynamics prior to and after the typhoon, (ii) examine shoreline movement and assess coastal erosion and accretion, (iii) assess the degree of typhoon damage to vegetated land, and (iv) analyze changes in SSC and the response of sediment dynamics over the typhoon period. Coastal managers can use this study to develop and implement appropriate strategies and practices to protect natural

https://doi.org/10.5194/nhess-2022-253
Preprint. Discussion started: 9 November 2022

Natural Hazards and Earth System Sciences
Discussions

ecosystems and post-disaster rehabilitation.

2. Study Area

The Mokpo coast is located in the southwestern part of South Korea and is characterized by muddy flats with wide tidal ranges (Choi et al., 2007; Kang et al., 2007), as depicted in Figure 1. The inner part of the coast includes harbor and industrial complexes, a large residential area, and a wastewater treatment plant. Mokpo coast is most frequently hit by typhoons, which cause the most significant amount of property damage and loss of human lives (Kang et al., 2020; Lee, 2014). According to storm surge records, the Mokpo coastal region has experienced the highest number of typhoons (58) since 1980 due to its geographical location (Lee et al., 2022; Kang et al., 2020). It has been observed that the tidal range is broader, with extreme high tide 60cm higher and the extreme low tide 43cm lower in the Mokpo coast (Lee et al., 2022; Kwon et al., 2019). This fluctuation resulted in significant flooding during the typhoon period. High water and waves severely damage the coastal structures and environment, especially during surges (Tsai et al., 2006). The Mokpo coastal region is characterized by a strong ebb dominant pattern because of its complex bathymetry, scattered islands and extensive tidal flats (Byun et al., 2004; Kang and Jun, 2003; Kang, 1999).

The vast tidal flat of the Mokpo coast serves as a habitat for many different species, has a large production capacity, and is highly regarded for its role in cleaning up pollution and controlling floods and typhoons (Lee et al., 2021; Na, 2004). Furthermore, the powerful storm has affected the coastal wetlands (mudflats) that serve as the primary spawning and nursery grounds for fish and other marine life. However, Choi (2014) observed that tidal flat systems in the Korean peninsula are actively responding to various phenomena, such as tides, waves, and typhoons. The wetland, coastal vegetation and coastline along the Mokpo coastal region have been disturbed due to the extreme climatic events. It has been observed that most typhoon passages severely impacted the tidal flat environment and caused morphodynamics along the Mokpo coast.

https://doi.org/10.5194/nhess-2022-253
Preprint. Discussion started: 9 November 2022

Natural Hazards and Earth System Sciences
Open Access
EGU
Discussions

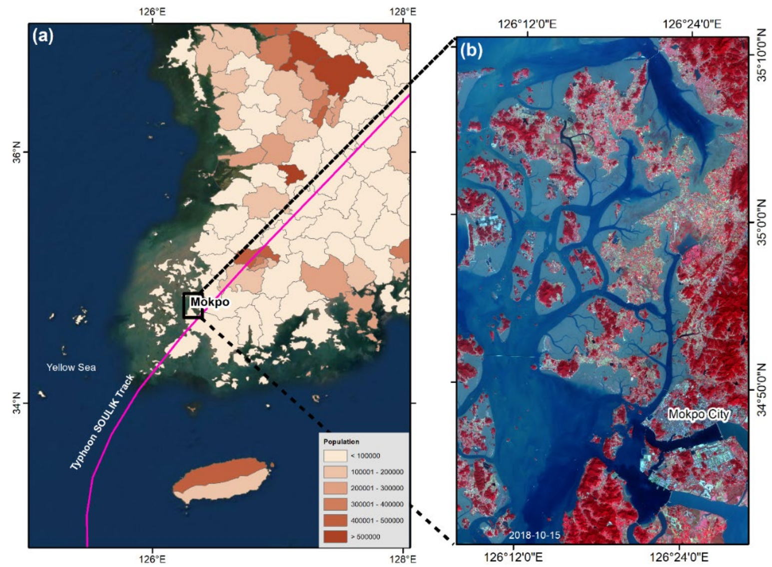

Figure 1. (a) Typhoon Soulik tracks pass through the Mokpo coastal region on 23rd August 2018 (Typhon track data is downloaded from https://www.ncdc.noaa.gov/ibtracs/, and basemap data are retrieved from ESRI World Imagery basemap), and (b) The post-typhoon Standard False Colour Composite of reflectance image of the Mokpo coastal region (Sentinel-2 MSI level 1C satellite images are downloaded from https://scihub.copernicus.eu/dhus/).

2.1 Typhoon Soulik

The southwestern coast of the Korean peninsula had been ravaged by the strong intensity typhoon Soulik, which hit the Mokpo coast on 23rd August 2018 (Ryang et al., 2018). On 16th August, it developed near Palau as a tropical depression. Subsequently, it strengthened into a tropical storm before intensifying into a typhoon (Lee et al., 2022). It moved into the East China Sea on 20th August with a maximum intensity of 950 hPa (44 m/s) and lasted until 22nd August. The intensity of typhoon Soulik was significantly over-predicted just before landfall on the Korean peninsula (Lee et al., 2022; Kang et al., 2020; Park et al., 2019). The Korea Meteorological Administration (KMA) issued typhoon warnings, and national and local authorities took preventative measures to limit potential damage. On 23rd August, around 14 UTC, Typhoon Soulik made landfall close to Mokpo City, located on Korea's southwest coast. It had a maximum sustained wind speed of 32 m/s and a central pressure of 975 hPa. It also dumped tremendous rain (Kand and Moon, 2022; Kang et al., 2020; Yu et al., 2018; Cha et al., 2021). The buoy station near Jeju Island has recorded extreme sea surface conditions, including a maximum wave height of 15m, gusts of 35 m/s, and a drop in water temperature of 10°C.

(Kang et al., 2020; Yoon et al., 2021). Furthermore, a significant wave height, i.e., 4-6 m, was also recorded along the Mokpo coast (Kang et al., 2020). In addition to causing flooding, the typhoon destroyed extensive vegetation with strong gusts and damaged non-residential structures. The total damage caused by Typhoon Soulik in South Korea was $45 million (KMA, 2018).

3. Data and Methods

3.1 Data Sources and pre-processing

Typhoon-induced coastal dynamics along the Mokpo coast have been studied using the pre-and post-event Sentinel-2 MSI images. A multispectral instrument (MSI), Sentinel-2 consists of two polar-orbiting satellites, Sentinel-2A and Sentinel-2B, which were launched in June 2015 and March 2017, respectively (ESA, 2020). The Sentinel 2 MSI has a 290 km wide field of view, a minimum revisits period of five days, 13 spectral bands ranging from visible to shortwave infrared (SWIR), and spatial resolution of 10m (4 bands), 20m (6 bands), & 60m (3 bands) (ESA, 2020). The Sentinel-2 User Manual describes the MSI's radiometric, spectral, and spatial characteristics (ESA, 2020).

The cloud-free Sentinel-2 MSI level 1C satellite images with a relatively fine spatial resolution (10m) for the pre-and post-typhoon period have been downloaded from the Copernicus Scientific Data Hub (https://scihub.copernicus.eu/dhus/). Level 1C is a 12-bit radiometric product that was presented the top of the atmospheric reflectance value (Phiri et al., 2019). The open-source software SNAP (Sentinel Application Platform) has been used to process the Sentinel-2 MSI images such as masking, band visualization, atmospheric correction etc. We used SANP’s iCOR tool (image correction for atmospheric effect) for atmospheric correction of the Sentinel 2 MSI data over the land and water (Tian et al., 2020; Keukelaere et al., 2018). Thereafter, satellite remote sensing reflectance (R_s) images have been used to monitor the coastal dynamics in the Mokpo coastal region over the typhoon period.

On the other hand, to exclude the impact of tidal changes, satellite images have been chosen during low tide conditions (Maiti and Bhattacharya, 2009). The tide height has been computed using the WXTide32 program (Hopper, 2004). Several researchers have discussed the significance of low tide satellite data for coastal mapping and dynamics modeling (Nayak, 2002). The details of pre- and post-typhoon satellite data used in the study are given in Table 1.

Table 1. The details of Sentinel-2 MSI data used for coastal dynamic modeling.

https://doi.org/10.5194/nhess-2022-253
Preprint. Discussion started: 9 November 2022

Natural Hazards and Earth System Sciences
Discussions

Periods	Date of acquisition	Sensor	Cloud cover (%)	Tidal Height (m)
Pre-typhoon	2018/08/01	Sentinel-2B MSI	1.3464	0.77
Post-typhoon	2018/10/15	Sentinel-2B MSI	0.6548	1.01

3.2. Typhoon-induced coastal dynamic modeling

This study aims to analyze the typhoon Soulik-induced coastal dynamics and associated coastal changes along the Mokpo coastal region. Figure 2 depicts an integrated flowchart of the impact of a typhoon on a coastal system. The outline of the study is divided into four sections: (a) coastal vegetation disturbance mapping, (b) coastal landform mapping and change analysis, (c) suspended sediment concentration variation modeling, and (d) coastal erosion and accretion analysis. The details methodology of each objective has been discussed in the subsequent section.

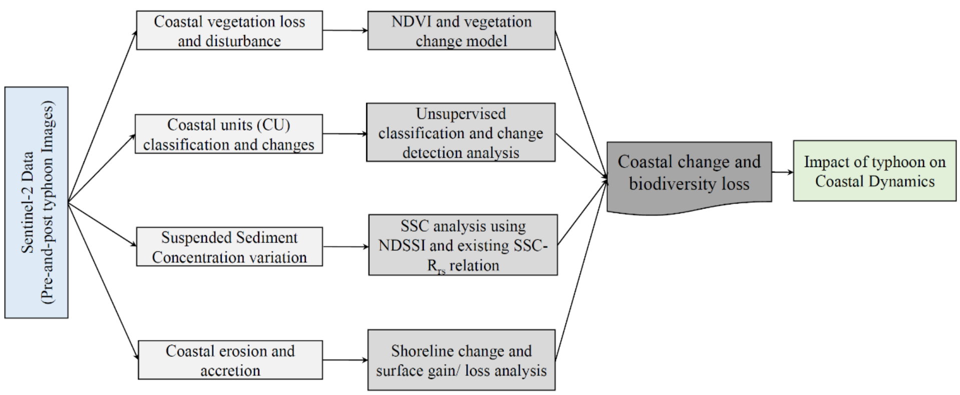

Figure 2. Geospatial-based approach for coastal dynamics due to a typhoon.

3.2.1 Analyses of coastal vegetation loss and disturbance

Vegetation damage severity mapping (VDSM) has been performed using pre-and post-event satellite images. NDVI is widely used for measuring vegetation density, health status, regional vegetation condition, and detecting vegetation disturbances (Xu et al., 2021; Mishra et al., 2021b; Wang et al., 2010; Yang et al., 2018). Numerous studies have shown that the NDVI is a reliable indicator of post-typhoon damage detection (Xu et al., 2021; Mishra et al., 2021a; Charrua et al., 2021; Shamsuzzoha et al., 2021; Kumar et al., 2021; Nandi et al., 2020; Wang and Xu, 2018; Konda et al., 2018; Zhang et al., 2013; Rodgers et al., 2009). Therefore, in this study, the vegetation damage before and after Typhoon Soulik has been determined using the NDVI approach. The NDVI has been calculated by using the following Eq. (1) (Rouse et al., 1973; Filgueiras et al., 2019):

$$NDVI = \frac{\rho\text{NIR} - \rho\text{RED}}{\rho\text{NIR} + \rho\text{RED}} \quad (1)$$

where, ρNIR and ρRED are the spectral reflectance corresponding to the eight (832.8–832.9nm) and fourth (664.6– 664.9nm) Sentinel-2 MSI bands, respectively (Xu et al., 2021). In general, NDVI values range from -1.0 to 1.0; the higher the NDVI value, the better the conditions for vegetation development, and extremely low values indicate the presence of water. Furthermore, the NDVI value above 0.4 indicates vegetated surfaces, and those between 0.25 and 0.40 signify soils with the presence of vegetation (Charrua et al., 2020). The vigor of the vegetation increases as the NDVI values come closer to 1.00 (Rouse et al., 1974). Numerous studies have established the NDVI threshold for vegetated land (e.g., Xu et al., 2021; Wong et al., 2019; Liu et al., 2015; Eastman et al., 2013; Yang et al., 2012; Sobrino et al., 2004). Most researchers noted that the NDVI threshold value for vegetation cover typically ranges from 0.15-2.0 (Xu et al., 2021; Eastman et al., 2013; Sobrino et al., 2004). Therefore, the vegetated pixels (e.g., NDVI threshold > 0.20) that are present in pre and post-typhoon NDVI images have been used for vegetation severity analysis. The NDVI threshold is considered to reduce the influence of land cover change from the pre-typhoon (2018-08-01) to post-typhoon (2018-10-15) periods.

The degree of vegetation damage has been determined by comparing the NDVI values of the pre-and post-typhoon periods. Various researchers have frequently used the direct difference of NDVI to determine the damage severity caused by typhoons to natural vegetated land (Wang and Xu, 2018; Konda et al., 2018). It has been calculated on a cell-by-cell basis by subtracting the pre-typhoon NDVI image from that of the post-typhoon, in ArcGIS software using map algebra (Zhang et al., 2013; Cakir et al., 2006). The following equation is used to calculate the ΔNDVI (Wang and Xu, 2018),

$$\Delta NDVI = NDVI_{post-typhoon} - NDVI_{pre-typhoon} \quad (2)$$

The difference in NDVI (i.e., ΔNDVI) illustrates the change in natural vegetation, while a negative ΔNDVI value indicates the damage inflicted by a typhoon to the vegetation cover (Xu et al., 2021).

The relative change in NDVI value has been used to investigate the geo-ecological impact on the forest area (Mishra et al., 2021b). The relative vegetation changes ($NDVI_r$) after

Soulik have been determined by using the following Eq. (3) (Kumar et al., 2021):

$$NDVI_r = \frac{\Delta NDVI}{NDVI_{pre-typhoon}} \times 100 \quad (3)$$

Where the negative $NDVI_r$ value, indicates vegetation loss caused by typhoons, and positive $NDVI_r$ value shows vegetation gain. The $NDVI_r$ value has been classified into three categories corresponding to pixels with decreased, no change, or increased vegetation cover.

3.2.2 Coastal landform classification and change analysis

Typhoons have adversely affected the coastal landform and ecology of the south and west coast of the Korean peninsula every year. Therefore, a GSI-based coastal change model has been developed to understand the morphodynamics of coastal landforms during typhoons. In the present study, we considered four coastal landform classes, i.e., wetland land, wetland vegetation, land, and water for the coastal morphodynamic analysis (Maiti and Bhattacharya, 2011). The method consists of two algorithms, i.e., (a) the ISODATA algorithm used to classify the coastal landform with four main classes, i.e., water, wetland, wetland vegetation, and land, and (b) the change detection technique used to quantify the pre- and post-typhoon coastal changes. In this approach, we accentuate in-depth morphological changes and emphasize minor changes along the Mokpo coast caused by typhoon Soulik.

The pre-and post-typhoon Sentinel-MSI images have been classified using the unsupervised classification technique to distinguish among different coastal landforms of the study region. This approach is used to determine which types of coastal landforms were adversely affected by Typhoon Soulik and which of them have recovered more quickly than others. Erdas Image software has been used to run the unsupervised classification algorithm (ERDAS, 1997). Based on the k-means algorithm, this technique reduces variability within pixel clusters (Charrua et al., 2021; Aswatha et al., 2020; Bhowmik et al., 2013). Finally, pre- and post-typhoon Sentinel-2 MSI images have been classified into four coastal landform classes: land, water, wetland, and wetland vegetation.

The accuracy assessment is a commonly used method to determine how closely the classified map matches the reference map (Congalton, 1991). In the present study, the classified data (i.e., coastal landforms maps) have been derived through an unsupervised classification technique, while 550 random samples collected from different parts of the Sentinel- 2MSI standard false-color image are considered reference data. Thereafter, a confusion matrix has been developed based on the reference and classified data to evaluate accuracy (Story and

https://doi.org/10.5194/nhess-2022-253
Preprint. Discussion started: 9 November 2022

Congalton, 1986). The kappa coefficient (*k*). has been used to determine the quantitative accuracy of the classified map (Landis and Koch, 1977). The assessment is quantified using three different statistics: overall accuracy, producer accuracy, and user accuracy (Jensen, 1996). The model's precision is classified into five categories based on the *k* values: near perfect ($k > 0.8$), substantial ($0.6 < k < 0.8$), moderate ($0.4 < k < 0.6$), fire ($0.2 < k < 0.4$), and poor ($k < 0.2$) (Landis and Koch, 1977).

The land transformation model based on mutual spatial replacements has been applied during the post-classification stage, as shown in Figure 3. The classified coastal landform classes, such as land, wetland, wetland vegetation, and water, have been replaced spatially in order to create coastal-change units. For example, the coastal landform class of 'wetland vegetation' in the pre-typhoon period replaced by 'water' in the post-typhoon period (Table 2) indicates the change class 'wetland vegetation replaced by water. A total of nine coastal-change classes have been derived, as illustrated in Table 2.

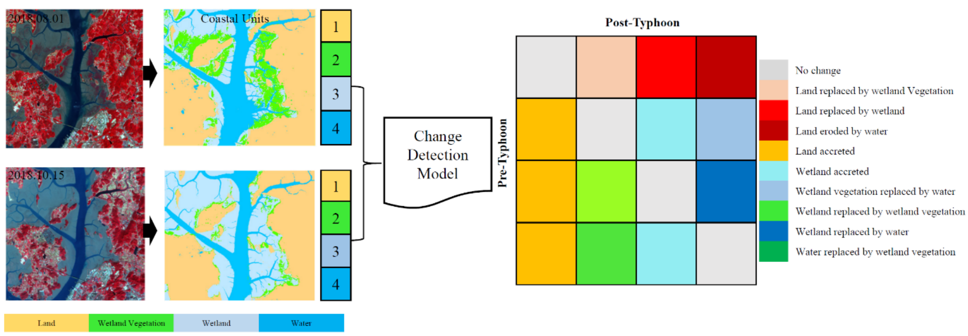

Figure 3. The Coastal-change model exhibits the spatial replacements among coastal landform classes.

Table 2. The coastal land transformation over the typhoon period.

Post-typhoon / Pre-typhoon	Land	Wetland Vegetation	Wetland	Water
Land	No change	Land replaced by wetland Vegetation	Land replaced by wetland	Land eroded by water
Wetland Vegetation	Land accreted	No change	Wetland accreted	Wetland vegetation replaced by water

Wetland	Land accreted	Wetland replaced by wetland vegetation	No change	Wetland replaced by water
Water	Land accreted	Water replaced by wetland vegetation	Wetland accreted	No Change

3.3 Suspended sediment concentration modeling

The suspended sediment concentration (SSC) distribution in coastal regions is a significant indicator of changes in the marine environment caused by typhoon-induced storm surges, strong waves, and subsequent coastal flooding (Min et al., 2012; Gong and Shen, 2009). In a short period, a typhoon may drastically influence the water column structures (Souza et al., 2001), change the transport and deposition of sediment (Li et al., 2015), and affect the distribution of nutrients and biological production (Wang et al., 2016) in the affected seas. Extreme storms or typhoons can modify suspended sediment distribution in coastal areas, which can significantly change marine habitats (Chau et al., 2021; Lu et al., 2018; Li land Li, 2016). Due to strong typhoon wind stress, the concentration of suspended particles in the seawater column and sediment resuspension may increase dozens of times before and after the event (Lu et al., 2018; Bian et al., 2017). Thus, typhoons significantly affect suspended sediment movement in the coastal region (Zhang et al., 2022; Li and Li, 2016; Goff et al., 2008). The spatiotemporal distribution of SSC can be impacted by variations in tidal phase, runoff, and wind speed (Tang et al., 2021). Furthermore, the resuspension of sediment can cause numerous problems to ocean engineering and change the ecology of the region (Kim, 2010). The amount of material delivered to and adverted across the shelf by typhoons is considerably larger than that of winter storm systems (Dail et al., 2007). The southern and western part of the Korean peninsula is affected by an average of three typhoons annually passing through the Yellow Sea (KMA, 2018; Altman et al., 2013). Some studies on SSC distribution impacted by artificial construction along the coastal region of the Yellow Sea have been undertaken by several researchers (i.e., Lee et al., 2020; Eom et al., 2016; Min et al., 2012, 2014; Choi et al., 2014). However, the effects of typhoons on the sedimentary environment in the Mokpo coastal region have not yet been investigated. Therefore, it is imperative to carry out regional-scale SSC mapping and coastal modifications to reveal changes in the marine environment and sediment transport mechanisms over the typhoon period.

Remote sensing has long contributed to the advancement of water quality studies (Hossain et al., 2021). In the present study, we attempted to calculate both the qualitative and

https://doi.org/10.5194/nhess-2022-253
Preprint. Discussion started: 9 November 2022

quantitative SSC in the inner-shelf region of the Mokpo coast using Sentinel-2B MSI data. The relative suspended sediment concentration has been calculated from pre- and post-typhoon Sentinel-2B MSI images using the Normalized Difference Suspended Sediment Index (NDSSI). NDSSI has been used in various water quality research (Kavan et al., 2022; Hossain et al., 2010). Further, many studies have successfully used Landsat and Sentinel-2 data to calculate NDSSI (Shahzad et al., 2018; Arisanty & Saputra, 2017). This index determines the relative concentration of suspended sediment, with values ranging from -1 to 1, where -1 indicates the highest concentration and +1 indicates the lowest (Hossain et al. 2010). The NDSSI has been calculated by using Eq. (4).

$$NDSSI = \frac{\rho\text{Blue} - \rho\text{NIR}}{\rho\text{Blue} + \rho\text{NIR}} \tag{4}$$

where, ρBlue and ρNIR represent the surface reflectances of Band 2 (492.1– 492.4 nm) and Band 8 (832.8 – 833.0 nm) of Sentinel-2 MSI data, respectively. The NDSSI is based on the observation that turbid waters reflect more in the NIR band but less in the visible band. The negative NDSSI value represents that the reflectance of water in the NIR band is greater than that in the blue band (Shahzad et al., 2018; Hossain et al., 2010). Therefore, the positive values of NDSSI represent lower SSC or more transparent water, while a negative value indicates higher SSC. The spatial patterns of relative SSC during the typhoon period have been determined using the NDSSI.

On the other hand, the empirical model has been used to quantify the suspended sediment concentration before and after typhoon Soulik. This method is widely used for SSC mapping and monitoring around the world (Eom et al., 2017; Hwang et al., 2016; Son et al., 2014; Min et al., 2012; Lee et al., 2011; Choi et al., 2014). For this purpose, we reviewed the existing relations between the in-situ SSC (SS, g/m3) and remote sensing reflectance (R_s) developed by various researchers for the southern and western coasts of South Korea, as illustrated in Table 3. In the present study, the SSC algorithm developed by Choi et al. (2014) for the Mokpo coastal region based on the in-situ SSC and a spectral ratio of water reflectance around 660nm has been used to quantify the SSC distribution. The atmospheric corrected sentinel-2 MSI image (RED band) has been used to calculate the SSC.

Table 3. Relationship between the remote sensing reflectance (R_r) and suspended sediment concentration (SS, g/m^3).

Authors	Relation	Region	Wavelength (nm)
Min et al. (2012)	$Y=0.24e^{188.3x}$	Saemangeum coastal	560nm

https://doi.org/10.5194/nhess-2022-253
Preprint. Discussion started: 9 November 2022

Min et al. (2006)		area	
Choi et al. (2014)	$Y=1.545e^{179.53x}$	Mokpo coastal, Gyeonggi Bay	660nm
Lee et al. (2011)	$Y=16.2064e^{15.3529x}$	Gwangyang Bay and Yeosu Bay	565nm
Choi et al. (2012) Lee et al. (2020)	$Y=1.7532e^{204.26x}$	Yellow Sea	660nm
Eom et al. (2017)	$Y=1.5119e^{179.85x}$	Nakdong River	660nm
Min et al. (2004)	$Y=0.99e^{199.9x}$	Saemangeum	560nm

3.4 Coastal erosion and accretion analysis

The shorelines (i.e., land and water boundary) of the Mopko coast for pre- and post-typhoon periods have been extracted using a semi-automatic technique (Maiti and Bhattacharya, 2011). Here, we used the normalized difference water index (NDWI) and manual digitization approach to separate the land and water boundary. The technique is widely used for dividing the land and water boundary (Santos et al., 2021; Dai et al., 2019). By using Sentinel-2 imagery, NDWI can be achieved with the following formula (McFeeters, 1996),

$$NDWI = \frac{\rho\text{Green} - \rho\text{NIR}}{\rho\text{Green} + \rho\text{NIR}} \quad (5)$$

where, ρGreen is the green band, and ρNIR is the near-infrared band of Sentinel-2 MSI data.

The extracted land and water boundary of the Mokpo region are then converted into polygons, and the shoreline has been determined using ArcGIS software. The shoreline change statistics have been calculated using the DSAS program (Thieler et al., 2009). The extracted shoreline for pre-and post-typhoon periods has been merged, and a 10m interval transect perpendicular to a baseline has been created (Santos et al., 2021). Thereafter, the NSM method has been used to calculate the total shoreline movement (in meters) between the pre-and post-typhoon shoreline positions of each transect (Kermani et al., 2016).

$$NSM = sh_{post} - sh_{pre} \quad (6)$$

Where, sh_{post} and sh_{pre} represent the post-typhoon shoreline position and pre-typhoon shoreline position, respectively.

On the other hand, the back-shore surface area changes due to shoreline movement (retreat/advance) over the typhoon period has also been calculated using the geo-statistical analyst tool. Several researchers have also previously mapped the surface changes of the backshore region (Awad and El-Sayed, 2021; Deabes, 2017; Karmani et al., 2016). In order to produce the surface area-change map, we generated two polygons, one for each shoreline and

https://doi.org/10.5194/nhess-2022-253
Preprint. Discussion started: 9 November 2022

Natural Hazards and Earth System Sciences
Discussions

then subtracted them from each other over the typhoon period. Finally, two feature classes have been derived, one for erosion and another for accretion. In addition, the attribute table contained in each zone illustrates the magnitude of spatial changes (amounts of erosion and accretion) during the typhoon period.

4. Result and Discussion

4.1 Vegetation damage severity mapping (VDSM) before and after typhoon

The VDSM shows the degree of vegetation damage due to typhoons. The comparison of pre-and post-typhoon NDVI distribution shows a significant loss of vegetated land as the number of no-productivity and/or low-productivity pixels increases in the post-typhoon NDVI image, as shown in Figure 4. Further, to determine the severity of vegetation damage, the pre- and post-typhoon NDVI image have been classified into six categories, namely non-vegetation (-1.0-0.0), low-vegetation (0.0-0.2), medium-low vegetation (0.2-0.4), medium vegetation (0.4-0.6), medium-high vegetation (0.6-0.8) and high vegetation (0.8-1.0).

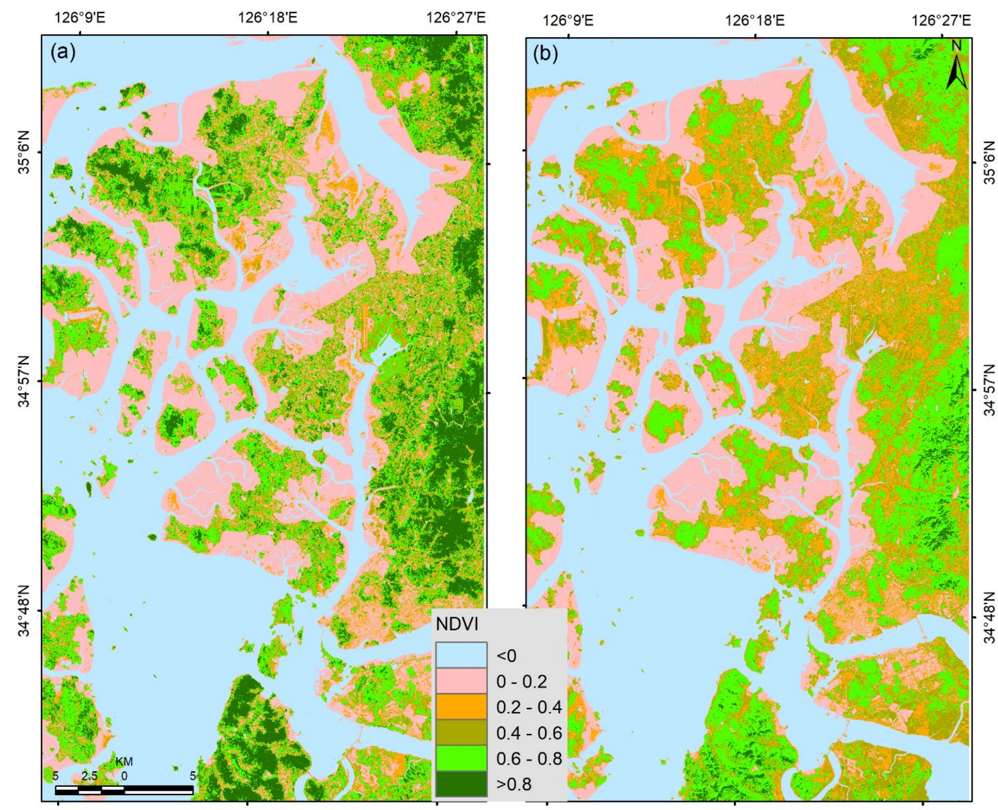

https://doi.org/10.5194/nhess-2022-253
Preprint. Discussion started: 9 November 2022

Natural Hazards and Earth System Sciences
Discussions

Figure 4. Status of vegetation greenness based on the NDVI data for the (a) pre-Soulik (01st August 2018) and post-Soulik (15th October 2018) period.

Table 4 depicts the area changes for each NDVI category during the typhoon period. It has been observed that the high NDVI values (>0.8) have changed drastically after typhoon-Soulik. The area changes in the Low and Non-vegetation categories along the Mokpo coastal region revealed that the wetland(mudflat) had accreted after the typhoon. On the other hand, the post-typhoon image was acquired two months after typhoon Soulik, which suggests that the grasses and crops have recovered well. This recovery is reflected in Table 4 from medium-low to medium-high NDVI levels.

Table 4. NDVI distribution over the study area before and after the typhoon.

NDVI levels	Pre-typhoon (sq.km)	Post-typhoon (sq.km)	Change (sq.km)
Non-vegetation (-1 to 0)	673.7337	647.5727	-26.161
Low (0 to 0.2)	430.0351	415.1584	-14.8767
Medium-low (0.2 to 0.4)	141.6401	243.2874	101.6473
Medium (0.4 to 0.6)	132.514	225.3398	92.8258
Medium-high (0.6 to 0.8)	283.6838	294.0909	10.4071
High (0.8 to 1.0)	183.6391	19.7964	-163.843

In order to determine the damaged vegetation areas along the Mokpo coast, we compared pre-and post-typhoon NDVI images. A decrease in ΔNDVI is one of the most distinctive features of abrupt canopy modifications detectable by optical remote sensing (Xu et al., 2021). Thus, we can only determine vegetation deterioration from the two NDVI images. Subsequently, an NDVI threshold of 0.2 has been used to extract only vegetation features from the pre-and post-typhoon NDVI images. The threshold value has been manually adjusted to achieve the highest accuracy of vegetation pixels. The extracted vegetated pixels have been compared with reference samples randomly collected from the original high spatial resolution images to determine the accuracy (Schneider, 2012; Xu et al., 2021). The two extracted vegetation images obtained within six or seven weeks of typhoon Soulik's (i.e., before the damaged vegetation had recovered) resulted an overall accuracy of 95.7 % for pre-typhoon and 94.5% for the post-typhoon period.

Figure 5 depicts the spatial distribution of ΔNDVI, where the highest ΔNDVI indicates a region with highly impacted vegetation areas. The negative ΔNDVI is attributed about 26.7% of the total area (1845.60 km2), which indicates that Typhoon Soulik affected approximately

https://doi.org/10.5194/nhess-2022-253
Preprint. Discussion started: 9 November 2022

Natural Hazards and Earth System Sciences
Discussions

479.9 km^2 of vegetated land. The lowest ΔNDVI value is -0.89, which indicates either tree wind-throw or a change in land surface cover from vegetation to build-up land or other non-vegetation covers (Zhang et al., 2013). The results showed that wetland vegetation and agricultural land experienced the most significant NDVI changes, with ΔNDVI values below-0.3. This suggests that these two types of land cover were severely affected by typhoon Soulik. It has been observed that the vegetation covers significantly decreased after the typhoon. The probable reason for the change is that Typhoon Soulik made landfall close to Mokpo coastal region.

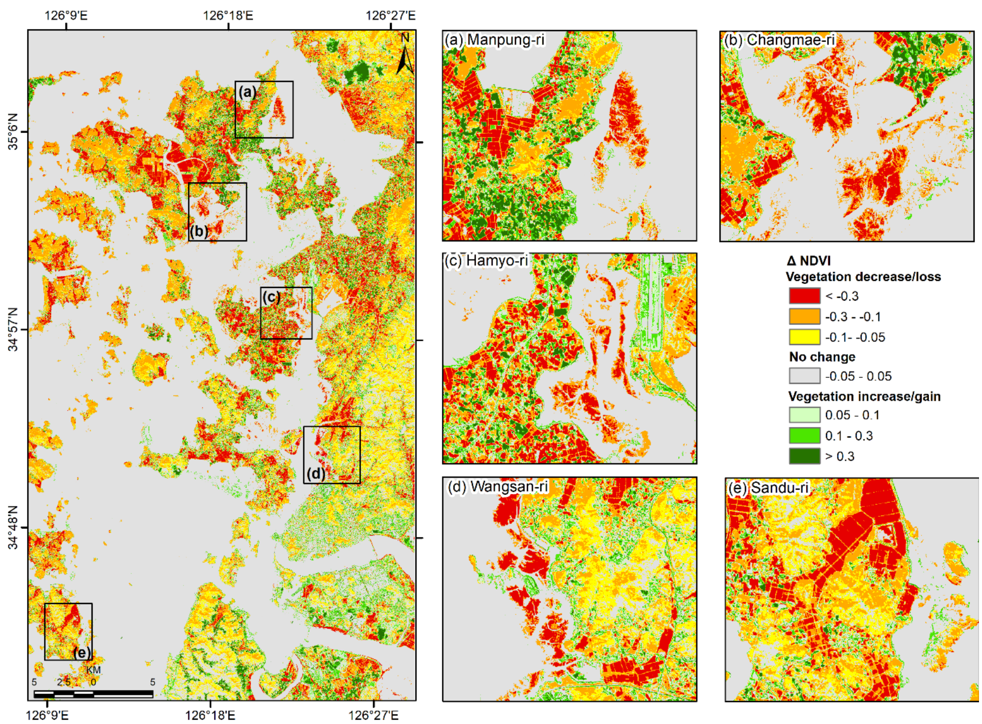

Figure 5. NDVI change map due to the typhoon Soulik of Mokpo coastal region, whereas zoom boxes show the vegetation damage of different sites: (a) Manpung-ri, (b) Changmae-ri, (c) Hamyo-ri, (d) Wangsan-ri, and (e) Sandu-ri.

The pre-and post-typhoon Sentinel-2 false-color images and the corresponding relative change in $NDVI_r$ values are presented in Figure 6. The dramatic vegetation loss (<-80%) (i.e., significant loss of vegetation) occurred in mostly wetland vegetation. In addition, moderate greenness loss has been identified in natural forests. Furthermore, the decrease of $NDVI_r$ values from higher classes to lower classes indicates that typhoon has severely damaged the low-lying

https://doi.org/10.5194/nhess-2022-253
Preprint. Discussion started: 9 November 2022

coastal regions and the wetland vegetation.

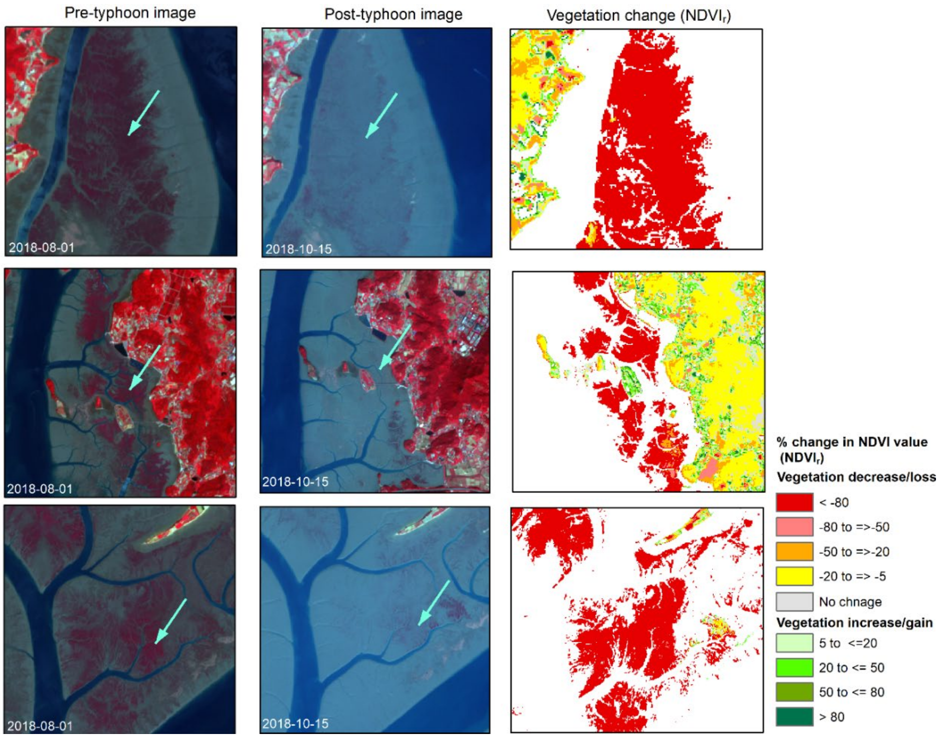

Figure 6. Sentinel-2 MSI standard false color composite images before and after Typhoon Soulik exhibits vegetation damage and the corresponding $NDVI_r$ (Sentinel-2 MSI level 1C satellite images are downloaded from https://scihub.copernicus.eu/dhus/).

4.2 Coastal morphodynamics over the typhoon period

To understand the coastal morphodynamics over the typhoon period, we classified the entire coastal region into four major coastal landform classes: land, wetland vegetation, wetland, and water (Fig. 7a-b). The accuracy and kappa coefficient of the classified maps exhibited a reasonable degree of consistency with the reference data, as illustrated in Table 5. The overall accuracy of the pre-and post-typhoon coastal landform maps was 86.5% and 84.3%, and kappa coefficients were 0.82 and 0.79, respectively. The results of the coastal landform classification showed a reduction in wetland vegetation over the typhoon period. Table 6 illustrates that before the typhoon, the area of the wetland vegetation class was 4.21% (77.63 km^2) of the total area of all categories (1845.60 km2). However, after the hitting of the typhoon storm, the wetland vegetation area reduced to 1.08 % (19.90 km^2), recording degradation of 57.73 km^2 (-74.37%).

https://doi.org/10.5194/nhess-2022-253
Preprint. Discussion started: 9 November 2022

Table 5. Accuracy assessment of pre-and post-typhoon classified coastal units.

Coastal Units	Description	Pre-typhoon		Post-typhoon	
		Producer Accuracy (%)	User Accuracy (%)	Producer Accuracy (%)	User Accuracy (%)
Land	Others Land use	90.2	92.0	91.9	90.7
Wetland vegetation	Wetland vegetation	83.4	84.0	85.0	83.3
Wetland	Mudflat/tidal flat	81.4	84.7	77.1	74.0
Water	Waterbody	91.4	85.3	83.2	89.3
Overall accuracy (%)		86.5		84.3	
kappa		0.82		0.79	

The class with the most remarkable gain was the wetland class after the typhoon. This is shown by an increase of wetlands from 258.14 km^2 to 334.97 km^2, i.e., an increase of 29.76% (76.83 km^2) during the analyzed period. Furthermore, the land class has increased by only 0.20% over the typhoon period, i.e., from 45.34% (before the typhoon) to 45.44% (after the typhoon). In addition, it has been noticed the waterbody decreased by 3.09% (20.78 km^2) after the typhoon. Thus, it can be inferred that most wetland vegetation and waterbody have been converted into wetlands, which caused the coastal deterioration.

Table 6. Coastal units for pre- and post-typhoon Soulik periods in the Mokpo coast.

Coastal Units	Area at pre-typhoon		Area at post-typhoon		Changed area	
	Sq.km	%	Sq.km	%	Sq.km	%
Land	836.87	45.34	838.55	45.44	1.68	0.20
Wetland Vegetation	77.63	4.21	19.90	1.08	-57.73	-74.37
Wetland	258.14	13.99	334.97	18.15	76.83	29.76
Water	672.95	36.46	652.18	35.34	-20.78	-3.09
Total	1845.60	100.00	1845.60	100.00	---	---

Thereafter, the coastal land transformation model has been developed through mutual spatial replacements between coastal units. The nine coastal-change units have been identified through the land transformation model, as shown in Figure 7(c). The results show that the low land coastal area drastically changed after the typhoon, where the majority of coastal classes have been transformed into wetlands or mudflats. Furthermore, approximately 9.77% of the land area has been replaced by wetland and water, whereas 65.52% of the wetland area has accreted over the wetland vegetation and water due to the impact of Soulik (Table 7).

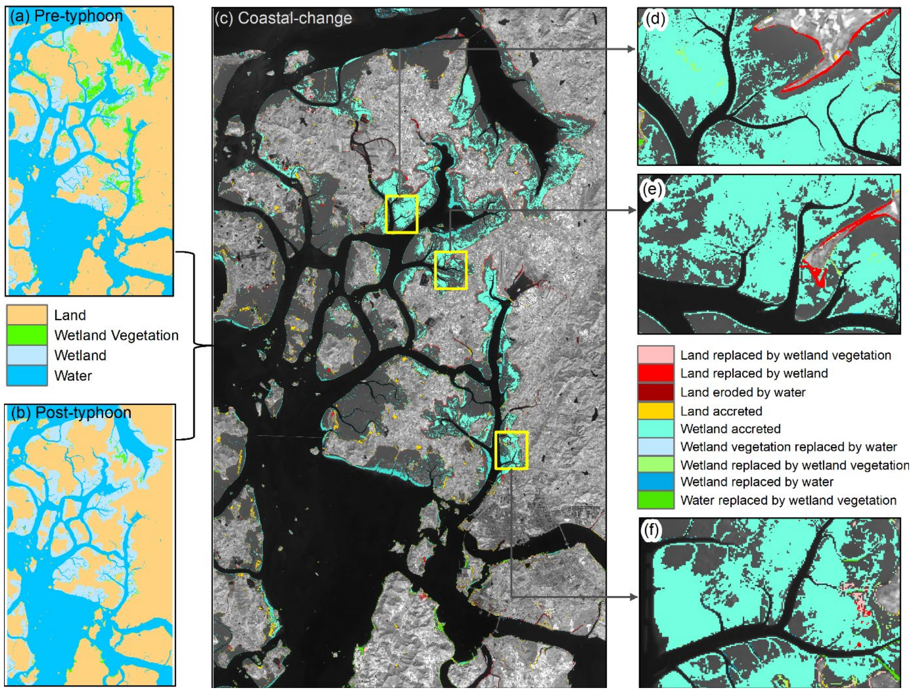

Figure 7. Spatial distribution of coastal-change units along the Mokpo coast due to typhoon Soulik (2018): (a) pre-typhoon classified map, (b) post-typhoon classified map, and (c) coastal land transformation map. Subplots (d, e, and f) show the detailed coastal land transformation.

Table 7. The details of coastal land transformation classes identify over the typhoon period.

Coastal land transformation	Area (km2)	%
Land replaced by wetland vegetation	4.59	6.86
Land replaced by wetland	4.41	6.60
Land eroded by water	2.12	3.17
Land accreted	3.29	4.92
Wetland accreted	43.79	65.52
Wetland vegetation replaced by water	2.47	3.70
Wetland replaced by wetland vegetation	1.59	2.38
Wetland replaced by water	1.76	2.64
Water replaced by wetland vegetation	2.82	4.22

4.3 Sediment resuspension during the pre-and post-typhoon period

The spatial distribution of relative suspended sediment concentration has been derived through NDSSI for both before and after typhoon images (Fig. 8). Pre-typhoon SSC patterns have been observed more inside the creeks of the inner-shelf region of the Mokpo coast as compared to the post-typhoon NDSSI image. However, it has been noted that the SSC has significantly increased along the entire coast in the post-typhoon period (Fig. 8b). Therefore, the spatial changes of relative SSC have been determined during the August (pre) and October (post) periods, as depicted in Figure 8(c). In general, a flood always transports many suspended materials and concentrates those materials on the upper surface of the water. After the strong events, the flood-transported suspended material is deposited across the delta. A similar phenomenon has been observed in the post-typhoon period due to extensive rainfall, which turned into a coastal flood.

On the other hand, it has been observed that the SSC gradually increased as the wind speed increased from the pre to post-typhoon period. The increasing SSC amplitudes indicate the rapid sediment erosion/resuspension over the storm passage. Furthermore, the amplitudes of SSC variations were more visible in shallower water than in deeper water. The effect of typhoons on the SSC variation along the Mokpo coast has been observed through ΔNDSSI distribution (Fig. 8c). The negative ΔNDSSI values represent the increase of SSC due to typhoon-induced strong wind and coastal flooding.

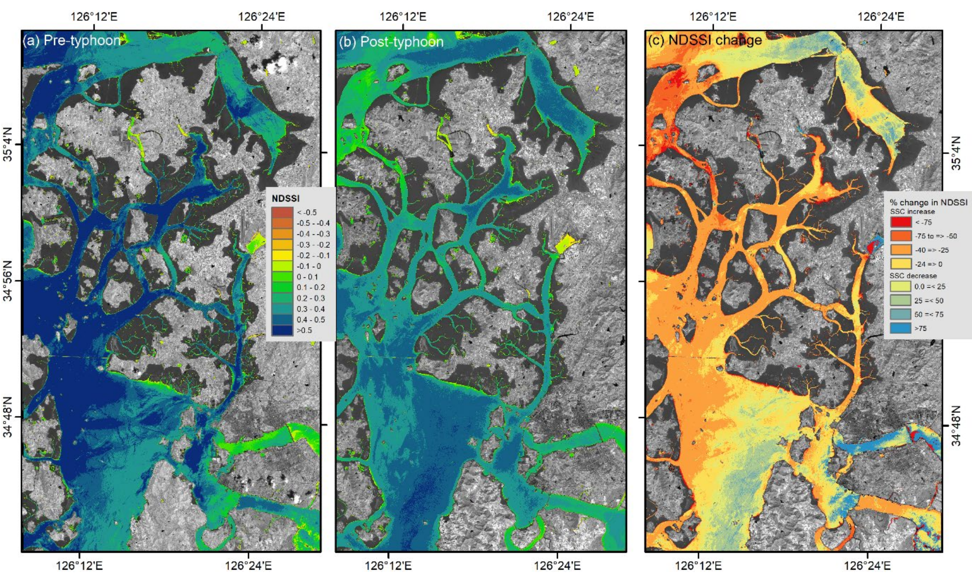

Figure 8. Relative SSC for (a) pre-typhoon and (b) post-typhoon period, while (c) represents the changes in the NDSSI.

Furthermore, a quantitative analysis of SSC has been performed based on the algorithm developed by Choi et al. (2014). During the pre-typhoon period, the SSC in the near shore waters was significantly higher than that of the offshore region (Fig. 9a). The post-typhoon

https://doi.org/10.5194/nhess-2022-253
Preprint. Discussion started: 9 November 2022

image shows a sharp increase in the SSC distribution, indicating that Typhoon Soulik significantly impacted the SSC variation, with a maximum of >50 g/m^3 (Fig. 9c). In Figures 9(a) and (b), the spring-neap tidal influence broadly regulated the distribution and change of SSC throughout the shallow coastal water. The resuspension of SSC has been observed in the entire study region during the passage of Soulik. The pattern of relative SSC distribution (Fig. 8c) and the empirically derived SSC distribution (Fig. 9c) of pre-and post-typhoon are similar.

The outcomes showed that the storm surge and strong waves have considerably aided the sediment resuspension. Thus, the storm waves played an essential role in increasing bottom stress and stirring the seabed sediment (Gong and Shen, 2009). The transport of sediment during the storm adds another mechanism to the long-term morphological evolution of the Mokpo coast. This research revealed the profound significance of typhoons on inner shelf sedimentation along the coast.

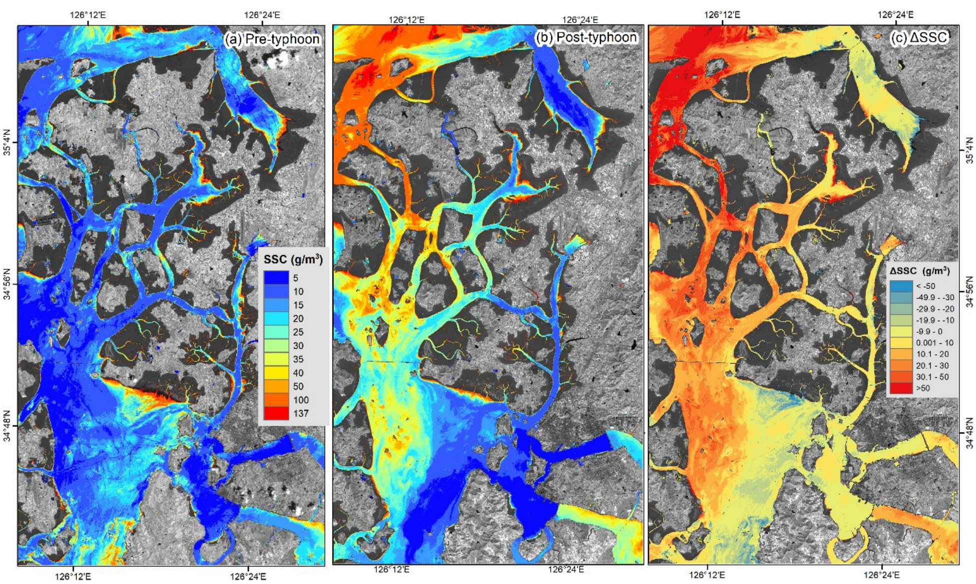

Figure 9. The simulated SSC distribution for the surface water of (a) pre-typhoon, (b) post-typhoon period, and (c) represents the spatial changes of SSC from pre- to post-typhoon.

4.4 Impact on coastal erosion and deposition

The impacts of the severe typhoon storm Soulik at a speed of 65 km/s on the coastline of Mokpo have been determined using the NSM method, considering 37,500 transects (10m transect intervals) along the shoreline. Figure 10 shows the shoreline alteration in the entire Mokpo coastal region from the pre- to post-typhoon period, with an accretion of 87.35%

https://doi.org/10.5194/nhess-2022-253
Preprint. Discussion started: 9 November 2022

Natural Hazards and Earth System Sciences
Open Access
EGU
Discussions

transects and erosion of 12.65%. The mean deposition of 16.98m and a mean erosion of -7.23m were recorded. The shoreline movement between 0-10m was recorded in the northern part of the coastal region. It has been observed that most transects experienced significant accretion, however, erosion has been observed in a few transects along the southern coastline (Fig. 10). The southern coast experienced the sporadic landward movement of the shoreline, while the rest of the study region experienced the significant seaward movement of the shoreline (Fig. 10 a-e).

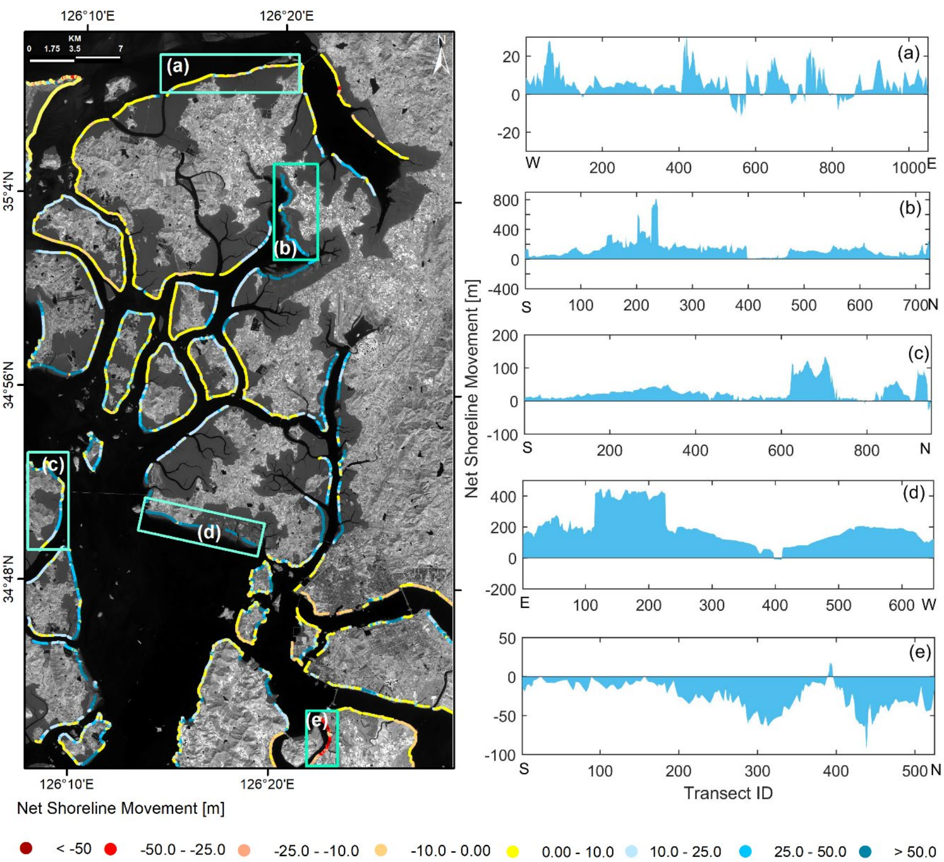

Figure 10. Land water boundary change from the pre-typhoon period to the post-typhoon period based on the NSM method (left panel). Subplots (a-e) show the net movement of the shoreline at different sites.

The wind generated surface water currents that transported and dispersed erogenous material to deep seas areas from pre- to post-typhoon. On the other hand, the coastal flooding induced by the typhoon storm increased the sediment from the land to the near-shore region

https://doi.org/10.5194/nhess-2022-253
Preprint. Discussion started: 9 November 2022

(Figs. 8c & 9c). This allowed sediment to deposit on the wetland or beach areas. The coastal land transformation map also revealed changes in shoreline shift-area as the wetland accreted class.

The net surface area changes along the coastal region have been estimated and are depicted in Figure 11. The total beach area increases and losses throughout the typhoon period were 16.23 km^2 and 1.1 km^2, respectively (Fig. 11f). It is observed that the wetland (mudflat) has been drastically increased by typhoon Soulik. These observations were also supported by other proxies, as discussed above.

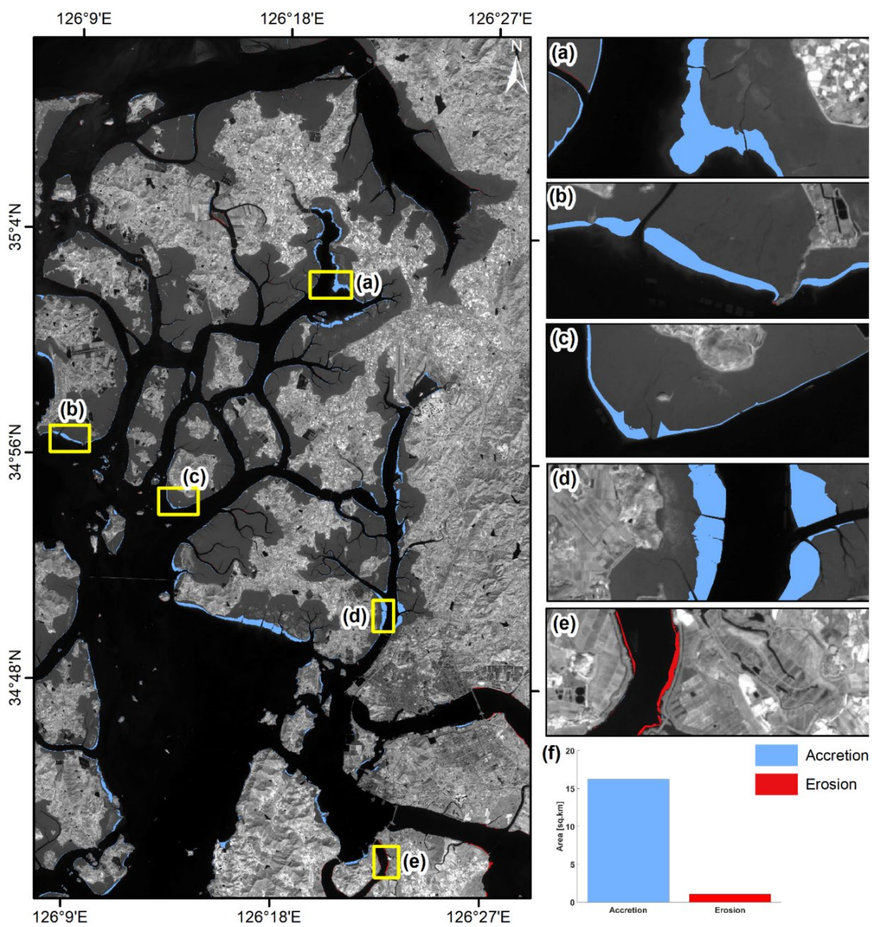

Figure 11. Gain and loss surface due to typhoon Soulik along the Mokpo coast. Subplots (a-d) show extensive accretion, while erosion is shown in plot (e). The bar graph (f) represents the area changes during the pre to post-typhoon period.

https://doi.org/10.5194/nhess-2022-253
Preprint. Discussion started: 9 November 2022

5. Conclusion

The objectives of this study were to assess the impact of typhoons Soulik on the coastal ecology, landform, erosion/accretion, suspended sediment movement and associated coastal changes along the Mokpo coast. This research developed an integrated approach for identifying coastal dynamics impacted by typhoons and determining damage severity. The coastline movement, coastal morphodynamics and quantified severity of vegetation damage from the pre- to post-typhoon period have been determined based on the Sentinel-2 MSI images. NDVI has been used to assess the severity of damage caused by typhoon Soulik on the vegetation. The results showed that about 493.9 km^2 (26.7%) of vegetation had been affected in the Mokpo coastal region. However, only 6.1% (112.4 km^2) of vegetated areas in low coastal land were severely damaged. The land transformation model exhibited that the 'wetland' replaced most of the 'wetland-vegetated land' in the post-typhoon period. Also, it has been found that more aggregated vegetation regions were less susceptible to damage.

The SSC of the Mokpo coastal region is higher in the post-typhoon period compared to pre-typhoon time. The SSC variation influenced the coastal accretion and changes the deltaic islands. The NDSSI and empirical-based SSC distribution of pre- and post-typhoon images exhibit sedimentation drastically increased after the typhoon. The land accretion process also dominated during the pre- to post-typhoon period. The wetlands and water have replaced approximately 9.77% of the land area. On the other hand, 65.52% of the wetland area has accreted over the wetland vegetation and water. Shoreline change analysis is also performed to understand erosion and accretion in coastal areas. The typhoon Soulik accelerated shoreline movement, affecting the local environmental condition, biodiversity imbalance, and aerial change. In addition, 87.35% of shoreline transects experienced seaward migration due to typhoon Soulik. The wetland experience accretion in a shorter period, but it made the coastline vulnerable to erosion in the near future because the natural native vegetation and wetland vegetation are crucial factors in shoreline stability of the coastal region due to its anti-erosive nature. It can be concluded that the Mokpo coastal ecosystem has been devastated by this extreme event. Although the observed changes are not alarming, shoreline protection measures still need to be addressed, especially the reforestation in wetland or mudflat regions. The outputs of the present study are needed to better understand the sediment transport process and estuary changes during the pre-and post-typhoon period. It can also be used to develop appropriate strategies to protect natural ecosystems and post-disaster rehabilitation.

Acknowledgments

The authors are thankful to the European Space Agency (ESA) for providing free satellite images.

Funding

This paper was supported by research funds for newly appointed professors of Gangneung-Wonju National University in 2021 and a grant (2021-MOIS35-003) of 'Policy-linked Technology Development Program on Natural Disaster Prevention and Mitigation' funded by the Ministry of Interior and Safety (MOIS, Korea).

References

Adhikari, M. D., Maiti, S., Bera, A., and Chaudhury, N. R.: Post-tsunami adjustment of coral reef platform and other morphometric changes in Landfall Island, North Andaman—An integrated field and remote sensing-based approach, Regional Studies in Marine Science, 48, 101975, https://doi.org/10.1016/j.rsma.2021.101975, 2021.

Altman, J., Doležal, J., Černý, T., and Song, J. S.: Forest response to increasing typhoon activity on the Korean peninsula: evidence from oak tree-rings, Global Change Biology, 19(2), 498-504, https://doi.org/10.1111/gcb.12067, 2013.

Arisanty, D., and Saputra, A. N.: Remote sensing studies of suspended sediment concentration variation in Barito Delta, In IOP Conference Series: Earth and Environmental Science, 98(1), 012058, 2017.

Aswatha, S. M., Mukherjee, J., Biswas, P. K., and Aikat, S.: Unsupervised classification of land cover using multi-modal data from multispectral and hybrid-polarimetric SAR imageries, International Journal of Remote Sensing, 41(14), 5277-5304, https://doi.org/10.1080/01431161.2020.1731771, 2020.

Awad, M., and El-Sayed, H. M.: The analysis of shoreline change dynamics and future predictions using automated spatial techniques: Case of El-Omayed on the Mediterranean coast of Egypt, Ocean & Coastal Management, 205, 105568, https://doi.org/10.1016/j.ocecoaman.2021.105568, 2021.

Bhowmik, A. K., and Cabral, P.: Cyclone Sidr impacts on the Sundarbans floristic diversity, Earth Science Research, 2(2), 62, http://dx.doi.org/10.5539/esr.v2n2p62, 2013.

Bhuiyan, Md. J. A. N. and Dutta, D.: Analysis of flood vulnerability and assessment of the

https://doi.org/10.5194/nhess-2022-253
Preprint. Discussion started: 9 November 2022

impacts in coastal zones of Bangladesh due to potential sea-level rise, Natural Hazards, 61(2), 729-743, https://doi.org/10.1007/s11069-011-0059-3, 2012.

Bian, S., Hu, Z., Liu, J., and Zhu, Z.: Sediment suspension and the dynamic mechanism during storms in the Yellow River Delta, Environmental Monitoring and Assessment, 189(1), 1-13, https://doi.org/10.1007/s10661-016-5688-2, 2017.

Bishop-Taylor, R., Nanson, R., Sagar, S., and Lymburner, L.: Mapping Australia's dynamic coastline at mean sea level using three decades of Landsat imagery, Remote Sensing of Environment, 267, 112734, https://doi.org/10.1016/j.rse.2021.112734, 2021.

Byun, D. S., Wang, X. H., and Holloway, P. E.: Tidal characteristic adjustment due to dyke and seawall construction in the Mokpo Coastal Zone, Korea, Estuarine, Coastal and Shelf Science, 59(2), 185-196, https://doi.org/10.1016/j.ecss.2003.08.007, 2004.

Cakir, H. I., Khorram, S., and Nelson, S. A.: Correspondence analysis for detecting land cover change, Remote Sensing of Environment, 102 (3-4), 306-317, https://doi.org/10.1016/j.rse.2006.02.023, 2006.

Cha, E. J., Yun, S. G., Moon, I. J., and Kim, D. H.: Binary interaction of typhoons Soulik and Cimaron in 2018–Part I: Observational characteristics and forecast error, Tropical Cyclone Research and Review, 10(1), 32-42, https://doi.org/10.1016/j.tcrr.2021.03.001, 2021.

Charrua, A. B., Padmanaban, R., Cabral, P., Bandeira, S., and Romeiras, M. M.: Impacts of the tropical cyclone idai in mozambique: A multi-temporal Landsat satellite imagery analysis, Remote Sensing, 13(2), 201, https://doi.org/10.3390/rs13020201, 2021.

Chau, P. M., Wang, C. K., and Huang, A. T.: The spatial-temporal distribution of GOCI-derived suspended sediment in Taiwan coastal water induced by typhoon Soudelor, Remote Sensing, 13(2), 194, https://doi.org/10.3390/rs13020194, 2021.

Choi, M. K., Choi, H. G., Moon, H. B., Yu, J., Kang, S. K., and Choi, S. K.: Sources and distributions of organic wastewater compounds on the Mokpo Coast of Korea, Fisheries and Aquatic Sciences, 10(4), 205-214, https://doi.org/10.5657/fas.2007.10.4.205, 2007.

Choi, J. K., Park, Y. J., Ahn, J. H., Lim, H. S., Eom, J., and Ryu, J. H.: GOCI, the world's first geostationary ocean color observation satellite, for the monitoring of temporal variability in coastal water turbidity, Journal of Geophysical Research: Oceans, 117(C9), https://doi.org/10.1029/2012JC008046, 2012.

Choi, J. K., Park, Y. J., Lee, B. R., Eom, J., Moon, J. E., and Ryu, J. H.: Application of the Geostationary Ocean Color Imager (GOCI) to mapping the temporal dynamics of

https://doi.org/10.5194/nhess-2022-253
Preprint. Discussion started: 9 November 2022

coastal water turbidity, Remote Sensing of Environment, 146, 24-35, https://doi.org/10.1016/j.rse.2013.05.032, 2014.

Choi, K.: Morphology, sedimentology and stratigraphy of Korean tidal flats–Implications for future coastal managements, Ocean & Coastal Management, 102, 437-448, https://doi.org/10.1016/j.ocecoaman.2014.07.009, 2014.

Congalton, R. G.: A review of assessing the accuracy of classifications of remotely sensed data, Remote Sensing of Environment, 37(1), 35-46, https://doi.org/10.1016/0034-4257(91)90048-B, 1991.

Dai, C, Howat, I. M., Larour, E., and Husby, E.: Coastline extraction from repeat high resolution satellite imagery, Remote Sensing of Environment, 229, 260–270, https://doi.org/10.1016/j.rse.2019.04.010, 2019.

Dail, M. B., Corbett, D. R., and Walsh, J. P.: Assessing the importance of tropical cyclones on continental margin sedimentation in the Mississippi delta region, Continental Shelf Research, 27(14), 1857-1874, https://doi.org/10.1016/j.csr.2007.03.004, 2007.

Datta, D. and Deb, S.: Analysis of coastal land use/land cover changes in the Indian Sunderbans using remotely sensed data, Geo-spatial Information Science, 15(4), 241-250, https://doi.org/10.1080/10095020.2012.714104, 2012.

Deabes, E. A.: Applying ArcGIS to Estimate the Rates of Shoreline and Back-Shore Area Changes along the Nile Delta Coast, Egypt, International Journal of Geosciences, 8(03), 332, DOI: 10.4236/ijg.2017.83017, 2017.

Eastman, J. R., Sangermano, F., Machado, E. A., Rogan, J., and Anyamba, A.: Global trends in seasonality of normalized difference vegetation index (NDVI), 1982–2011, Remote Sensing, 5(10), 4799-4818, https://doi.org/10.3390/rs5104799, 2013.

Eom, J., Lee, C., Jang, J., Choi, J. K., and Park, S.: Study on environmental change monitoring between shoreline change and suspended sediment concentration using Landsat images in Nakdong river, Korea, In IEEE International Geoscience and Remote Sensing Symposium (IGARSS), 3607-3609, 2017.

ERDAS.: ERDAS Imagine Tour Guides (Atlanta, GA: ERDAS Inc.), 1997.

ESA.: Multispectral instrument (MSI) overview, Retrieved 07th September, 2022, from https://sentinels.copernicus.eu/web/sentinel/technical-guides/sentinel-2-msi, 2020.

Filgueiras, R., Mantovani, E. C., Althoff, D., Fernandes Filho, E. I., and Cunha, F. F. D.: Crop NDVI monitoring based on sentinel 1, Remote Sensing, 11(12), 1441, https://doi.org/10.3390/rs11121441, 2019.

Goff, J. A., Allison, M. A., and Gulick, S. P.: Offshore transport of sediment during cyclonic storms: Hurricane Ike (2008), Texas Gulf Coast, USA, Geology, 38(4), 351-354, https://doi.org/10.1130/G30632.1, 2010.

Gong, W. and Shen, J.: Response of sediment dynamics in the York River Estuary, USA to tropical cyclone Isabel of 2003, Estuarine, Coastal and Shelf Science, 84(1), 61-74, https://doi.org/10.1016/j.ecss.2009.06.004, 2009.

Halder, B. and Bandyopadhyay, J.: Monitoring the tropical cyclone 'Yass' and 'Amphan'affected flood inundation using Sentinel-1/2 data and Google Earth Engine, Modeling Earth Systems and Environment, 1-16, https://doi.org/10.1007/s40808-022-01359-w, 2022.

Hopper, M.: WXTide32 Version 4.0. Free Software Foundation Inc., Cambridge, 2004.

Hoque, M. A. A., Phinn, S., Roelfsema, C., and Childs, I.: Assessing tropical cyclone impacts using object-based moderate spatial resolution image analysis: a case study in Bangladesh, International Journal of Remote Sensing, 37(22), 5320-5343, https://doi.org/10.1080/01431161.2016.1239286, 2016.

Hossain, A. K. M. A., Jia, Y., and Chao, X.: Development of remote sensing based index for estimating/mapping suspended sediment concentration in river and lake environments, In Proceedings of 8th international symposium on ECOHYDRAULICS, 435, 578-585, 2010.

Hossain, A. A., Mathias, C., and Blanton, R.: Remote sensing of turbidity in the Tennessee River using Landsat 8 satellite, Remote Sensing, 13(18), 3785, https://doi.org/10.3390/rs13183785, 2021.

Hu, T. and Smith, R. B.: The impact of Hurricane Maria on the vegetation of Dominica and Puerto Rico using multispectral remote sensing, Remote Sensing, 10(6), 827, https://doi.org/10.3390/rs10060827, 2018.

Hwang, D. J., Choi, J. K., Eom, J., Ryu, J. H., and Woo, H. J.: Long-term monitoring of suspended sediments concentration using GOCI and field data in Han-river estuary, Korea, In 2016 IEEE International Geoscience and Remote Sensing Symposium, 2465-2467, 2016.

Hwang, S., Son, S., Lee, C., and Yoon, H. D.: Quantitative assessment of inundation risks from physical contributors associated with future storm surges: a case study of Typhoon Maemi (2003), Natural Hazards, 104(2), 1389-1411, https://doi.org/10.1007/s11069-020-04225-z, 2020.

Kang, J. W.: Changes in tidal characteristics as a result of the construction of sea-dike/sea-walls in the Mokpo coastal zone in Korea, Estuarine, Coastal and Shelf Science, 48 (4), 429-438, https://doi.org/10.1006/ecss.1998.0464, 1999.

Kang, J. W. and Jun, K. S.: Flood and ebb dominance in estuaries in Korea, Estuarine, Coastal and Shelf Science, 56 (1), 187-196, https://doi.org/10.1016/S0272-7714(02)00156-7, 2003.

Kang, J. W., Moon, S. R., Lee, D. S., and Lee, J. L.: Surge-Wave Combined Inundation at Mokpo North Harbour, Korea, Journal of Coastal Research, 1081-1085, 2007.

Kang, K., Jo, H. J., and Kim, Y.: Ocean responses to Typhoon Soulik (1819) around Korea, Ocean Science Journal, 55(3), 445-457, https://doi.org/10.1007/s12601-020-0030-x, 2020.

Kang, K. and Moon, I. J.: Sea Surface Height Changes due to the Tropical Cyclone-Induced Water Mixing in the Yellow Sea, Korea, Frontiers of Earth Science, 10, 826582, doi: 10.3389/feart.2022.826582, 2022.

Kavan, J., Wieczorek, I., Tallentire, G. D., Demidionov, M., Uher, J., and Strzelecki, M. C.: Estimating Suspended Sediment Fluxes from the Largest Glacial Lake in Svalbard to Fjord System Using Sentinel-2 Data: Trebrevatnet Case Study, Water, 14(12), 1840, https://doi.org/10.3390/w14121840, 2022.

Kermani, S., Boutiba, M., Guendouz, M., Guettouche, M. S., and Khelfani, D.: Detection and analysis of shoreline changes using geospatial tools and automatic computation: Case of jijelian sandy coast (East Algeria), Ocean & Coastal Management, 132, 46-58, https://doi.org/10.1016/j.ocecoaman.2016.08.010, 2016.

Keukelaere, L. De, Sterckx, S., Adriaensen, S., Knaeps, E., Reusen, I., Giardino, C., ... and Vaiciute, D.: Atmospheric correction of Landsat-8/OLI and Sentinel-2/MSI data using iCOR algorithm: validation for coastal and inland waters, European Journal of Remote Sensing, 51(1), 525-542, https://doi.org/10.1080/22797254.2018.1457937, 2018.

Kim, Y. C.: Handbook of coastal and ocean engineering, World Scientific, 2010.

Kim, J. M., Bae, J., Son, S., Son, K., and Yum, S. G.: Development of model to predict natural disaster-induced financial losses for construction projects using deep learning techniques. Sustainability, 13(9), 5304, https://doi.org/10.3390/su13095304, 2021.

KMA.: Typhoon White Book, Available at https://www.kma.go.kr/download_01/typhoon/typwhitebook_2011.pdf, 2011.

KMA.: 2018 annual report, available at https://www.kma.go.kr/download_01/Annual

_Report_2018.pdf , 2018.

Konda, V. G. R. K., Chejarla, V. R., Mandla, V. R., Voleti, V., and Chokkavarapu, N.: Vegetation damage assessment due to Hudhud cyclone based on NDVI using Landsat-8 satellite imagery, Arabian Journal of Geosciences, 11(2), 1-11, https://doi.org/10.1007/s12517-017-3371-8, 2018.

Kumar, R., Rani, S., and Maharana, P.: Assessing the impacts of Amphan cyclone over West Bengal, India: a multi-sensor approach, Environmental Monitoring and Assessment, 193(5), 1-21, https://doi.org/10.1007/s10661-021-09071-5, 2021.

Kwon, J. I., Choi, J. W., Lee, J. C., Min, I. K., and Park, K. S.: Spatio-temporal Characteristics of Storm Surge Events in the Korean Peninsula, Journal of Coastal Research, 85 (10085), 891-895, 2018.

Landis, J. R. and Koch, G. G.: An application of hierarchical kappa-type statistics in the assessment of majority agreement among multiple observers, Biometrics, 363-374, 1977.

Lee, J. K., Kim, J. O., and Oh, Y. S.: Development of Coastal Safety Mapping System by Vulnerability Assessment of Tidal Creeks, Journal of Coastal Research, 114, 459-463, 2021.

Lee, M. S., Park, K., Chung, J. Y., Ahn, Y. H., and Moon, J. E.: Estimation of coastal suspended sediment concentration using satellite data and oceanic in-situ measurements, Korean Journal of Remote Sensing, 27(6), 677-692, 2011.

Lee, S. W., Nam, S. H., and Kim, D. J.: Estimation of marine winds in and around typhoons using multi-platform satellite observations: Application to Typhoon Soulik (2018), Frontiers of Earth Science, 16(1), 175-189, https://doi.org/10.1007/s11707-020-0849-6, 2022.

Lee, Y.: 2014. Coastal planning strategies for adaptation to sea level rise: A case study of Mokpo, Korea, Journal of Building Construction and Planning Research, 2(1), DOI:10.4236/jbcpr.2014.21007, 2014.

Lee, Y. K., Choi, J. K., and Lee, H. J.: A study on seasonal dynamics of suspended particulate matter in Korean coastal waters using GOCI, Journal of Coastal Research, 102 (SI), 232-245, https://doi.org/10.2112/SI102-029.1, 2020.

Li, K. and Li, G. S.: Risk assessment on storm surges in the coastal area of Guangdong Province, Natural Hazards, 68(2), 1129-1139, https://doi.org/10.1007/s11069-013-0682-2, 2013.

https://doi.org/10.5194/nhess-2022-253
Preprint. Discussion started: 9 November 2022

Li, Y., Li, H., Qiao, L., Xu, Y., Yin, X., and He, J.: Storm deposition layer on the Fujian coast generated by Typhoon Saola (2012), Scientific reports, 5(1), 1-7, https://doi.org/10.1038/srep14904, 2015.

Li, Y. and Li, X.: Remote sensing observations and numerical studies of a super typhoon-induced suspended sediment concentration variation in the East China Sea, Ocean Modelling, 104, 187-202, https://doi.org/10.1016/j.ocemod.2016.06.010, 2016.

Liu, Y., Wu, L., and Yue, H.: Biparabolic NDVI-Ts space and soil moisture remote sensing in an arid and semi-arid area, Canadian Journal of Remote Sensing, 41(3), 159-169, https://doi.org/10.1080/07038992.2015.1065705, 2015.

Lu, J., Jiang, J., Li, A., and Ma, X.: Impact of Typhoon Chan-hom on the marine environment and sediment dynamics on the inner shelf of the East China Sea: In-situ seafloor observations, Marine Geology, 406, 72-83, https://doi.org/10.1016/j.margeo.2018.09.009, 2018.

Maiti, S. and Bhattacharya, A. K.: A three-unit-based approach in coastal-change studies using Landsat images, International Journal of Remote Sensing, 32(1), 209-229, https://doi.org/10.1080/01431160903439965, 2011.

Mallick, B., Ahmed, B., and Vogt, J.: Living with the risks of cyclone disasters in the south-western coastal region of Bangladesh, Environments, 4(1), 13, https://doi.org/10.3390/environments4010013, 2017.

McFeeters, S. K.: The use of the Normalized Difference Water Index (NDWI) in the delineation of open water features, International Journal of Remote Sensing, 17(7), 1425–1432, https://doi.org/10.1080/01431169608948714, 1996.

Min, J. E., Ryu, J. H., Ahn, Y. H., and Lee, K. S.: Monitoring suspended sediment distribution using Landsat TM/ETM+ data in coastal waters of Seamangeum, Korea, In Proceedings of the KSRS Conference, The Korean Society of Remote Sensing, 340-343, 2004.

Min, J. E., Ahn, Y. H., Lee, K. S., and Ryu, J. H.: Development of Suspended Sediment Algorithm for Landsat TM/ETM+ in Coastal Sea Waters-A Case Study in Saemangeum Area, Korean Journal of Remote Sensing, 22(2), 87-99, 2006.

Min, J. E., Ryu, J. H., Lee, S., and Son, S.: Monitoring of suspended sediment variation using Landsat and MODIS in the Saemangeum coastal area of Korea, Marine Pollution Bulletin, 64(2), 382-390, https://doi.org/10.1016/j.marpolbul.2011.10.025, 2012.

Min, J. E., Choi, J. K., Yang, H., Lee, S., and Ryu, J. H.: Monitoring changes in suspended sediment concentration on the southwestern coast of Korea, Journal of Coastal

https://doi.org/10.5194/nhess-2022-253
Preprint. Discussion started: 9 November 2022

Research, 70, 133-138, 2014.

Mishra, M., Acharyya, T., Santos, C. A. G., da Silva, R. M., Kar, D., Kamal, A. H. M., and Raulo, S.: Geo-ecological impact assessment of severe cyclonic storm Amphan on Sundarban mangrove forest using geospatial technology, Estuarine, Coastal and Shelf Science, 260, 107486, https://doi.org/10.1016/j.ecss.2021.107486, 2021a.

Mishra, M., Santos, C. A. G., da Silva, R. M., Rana, N. K., Kar, D., and Parida, N. R.: Monitoring vegetation loss and shoreline change due to tropical cyclone Fani using Landsat imageries in Balukhand-Konark Wildlife Sanctuary, India, Journal of Coastal Conservation, 25(6), 1-11, https://doi.org/10.1007/s11852-021-00840-5, 2021b.

Moon, I. J., Oh, I. S., Murty, T., and Youn, Y. H.: Causes of the unusual coastal flooding generated by Typhoon Winnie on the west coast of Korea, Natural Hazards, 29(3), 485-500, https://doi.org/10.1023/A:1024798718572, 2003.

Na, C. K.: Heavy metals in sediments and organisms from tidal flats along the Mokpo coastal area, Economic and Environmental Geology, 37(3), 335-345, 2004.

Nandi, G., Neogy, S., Roy, A. K., and Datta, D.: Immediate disturbances induced by tropical cyclone Fani on the coastal forest landscape of eastern India: A geospatial analysis, Remote Sensing Applications: Society and Environment, 20, 100407, https://doi.org/10.1016/j.rsase.2020.100407, 2020.

Nayak, S.: Use of satellite data in coastal mapping, Indian Cartographer, 22(147-157), 1, 2002.

Parida, B. R., Behera, S. N., Oinam, B., Patel, N. R., and Sahoo, R. N.: Investigating the effects of episodic Super-cyclone 1999 and Phailin 2013 on hydro-meteorological parameters and agriculture: An application of remote sensing, Remote Sensing Applications: Society and Environment, 10, 128-137, https://doi.org/10.1016/j.rsase.2018.03.010, 2018.

Park, J. H., Yeo, D. E., Lee, K., Lee, H., Lee, S. W., Noh, S., ..., and Nam, S.: Rapid decay of slowly moving Typhoon Soulik (2018) due to interactions with the strongly stratified northern East China Sea, Geophysical Research Letters, 46(24), 14595-14603, https://doi.org/10.1029/2019GL086274, 2019.

Phiri, D., Simwanda, M., and Nyirenda, V.: Mapping the impacts of cyclone Idai in Mozambique using Sentinel-2 and OBIA approach, South African Geographical Journal, 103(2), 237-258, https://doi.org/10.1080/03736245.2020.1740104, 2021.

Rodgers, J. C., Murrah, A. W., and Cooke, W. H.: The impact of Hurricane Katrina on the coastal vegetation of the Weeks Bay Reserve, Alabama from NDVI data, Estuaries and

Coasts, 32(3), 496-507, https://doi.org/10.1007/s12237-009-9138-z, 2009.

Rouse, J. W., Haas, J. R. H., Schell, J. A., and Deering, D. W.: Monitoring vegetation systems in the Great Plains with ERTS, In Proceedings of the 3rd ERTS Symposium, Washington, DC, USA, 1, 1974.

Ryang, W. H., Kang, S. I., and Cho, K. S.: Characteristics of Surface Topography and Sediments before and after the Typhoon Soulik in 2018, Macrotidal Coast of Gochang, Korea, In AGU Fall Meeting Abstracts, OS33B-02, 2021.

Sadik, M., Nakagawa, H., Rahman, M., Shaw, R., Kawaike, K., and Parvin, G. A.: Assessment of cyclone Aila recovery progress in Bangladesh: a comparison between rice and shrimp farming villages in Koyra, In Water, Flood Management and Water Security Under a Changing Climate, Springer, Cham, 109-124, 2020.

Sahoo, B. and Bhaskaran, P. K.: Multi-hazard risk assessment of coastal vulnerability from tropical cyclones–A GIS based approach for the Odisha coast, Journal of Environmental Management, 206, 1166-1178, https://doi.org/10.1016/j.jenvman.2017.10.075, 2018.

Santos, C. A. G., do Nascimento, T. V. M., Mishra, M., and da Silva, R. M.: Analysis of long- and short-term shoreline change dynamics: A study case of João Pessoa city in Brazil, Science of the Total Environment, 769, 144889, https://doi.org/10.1016/j.scitotenv.2020.144889, 2021.

Schneider, A.: Monitoring land cover change in urban and peri-urban areas using dense time stacks of Landsat satellite data and a data mining approach, Remote Sensing of Environment, 124, 689-704, https://doi.org/10.1016/j.rse.2012.06.006, 2012.

Shahzad, M. I., Meraj, M., Nazeer, M., Zia, I., Inam, A., Mehmood, K., and Zafar, H.: Empirical estimation of suspended solids concentration in the Indus Delta Region using Landsat-7 ETM+ imagery, Journal of Environmental Management, 209, 254-261., https://doi.org/10.1016/j.jenvman.2017.12.070, 2018.

Shamsuzzoha, M., Noguchi, R., and Ahamed, T.: Damaged area assessment of cultivated agricultural lands affected by cyclone bulbul in coastal region of Bangladesh using Landsat 8 OLI and TIRS datasets, Remote Sensing Applications: Society and Environment, 23, 100523, https://doi.org/10.1016/j.rsase.2021.100523, 2021.

Sobrino, J. A., Jiménez-Muñoz, J. C., and Paolini, L.: Land surface temperature retrieval from LANDSAT TM 5, Remote Sensing of Environment, 90(4), 434-440, https://doi.org/10.1016/j.rse.2004.02.003, 2004.

https://doi.org/10.5194/nhess-2022-253
Preprint. Discussion started: 9 November 2022

Son, S., Kim, Y. H., Kwon, J. I., Kim, H. C., and Park, K. S.: Characterization of spatial and temporal variation of suspended sediments in the Yellow and East China Seas using satellite ocean color data, GIScience & Remote Sensing, 51(2), 212-226, https://doi.org/10.1080/15481603.2014.895580, 2014.

Souza, A. J., Dickey, T. D., and Chang, G. C.: Modeling water column structure and suspended particulate matter on the Middle Atlantic continental shelf during the passages of Hurricanes Edouard and Hortense, Journal of Marine Research, 59(6), 1021-1045, https://doi.org/10.1357/00222400160497751, 2001.

Story, M. and Congalton, R. G.: Accuracy assessment: a user's perspective, Photogrammetric Engineering and Remote Rensing, 52(3), 397-399, 1986.

Tang, R., Shen, F., Ge, J., Yang, S., and Gao, W.: Investigating typhoon impact on SSC through hourly satellite and real-time field observations: A case study of the Yangtze Estuary, Continental Shelf Research, 224, 104475, https://doi.org/10.1016/j.csr.2021.104475, 2021.

Thieler, E. R., Himmelstoss, E. A., Zichichi, J. L., and Ergul, A.: The Digital Shoreline Analysis System (DSAS) version 4.0-an ArcGIS extension for calculating shoreline change (No. 2008-1278), US Geological Survey, 2009.

Tian, Y., Mingming, J., Zongming, W., Dehua, M., Baojia, D., and Chao, W.: Monitoring invasion process of Spartina alterniflora by seasonal Sentinel-2 imagery and an object-based random forest classification, Remote Sensing, 12(9), 1383, https://doi.org/10.3390/rs12091383, 2020.

Tsai, C. H., Tzang, S. Y., Hsiao, S. S., Cheng, C. C., and Li, H. W.: Coastal structure failures and coastal waves on the north coast of Taiwan due to typhoon Herb, Journal of Coastal Research, 22(2), 393-405, 2006.

Tsai, Y. L. S.: Monitoring 23-year of shoreline changes of the Zengwun Estuary in Southern Taiwan using time-series Landsat data and edge detection techniques, Science of The Total Environment, 156310, https://doi.org/10.1016/j.scitotenv.2022.156310, 2022.

Wang, W., Qu, J. J., Hao, X., Liu, Y., and Stanturf, J. A.: Post-hurricane forest damage assessment using satellite remote sensing, Agricultural and forest meteorology, 150(1), 122-132, https://doi.org/10.1016/j.agrformet.2009.09.009, 2010.

Wang, T., Liu, G., Gao, L., Zhu, L., Fu, Q., and Li, D.: Biological and nutrient responses to a typhoon in the Yangtze Estuary and the adjacent sea, Journal of Coastal Research, 32(2), 323-332, 2016.

Wang, M. and Xu, H.: Remote sensing-based assessment of vegetation damage by a strong typhoon (Meranti) in Xiamen Island, China, Natural Hazards, 93(3), 1231-1249, https://doi.org/10.1007/s11069-018-3351-7, 2018.

Wang, S., Mu, L., Qi, M., Yu, Z., Yao, Z., and Zhao, E.: Quantitative risk assessment of storm surge using GIS techniques and open data: A case study of Daya Bay Zone, China, Journal of Environmental Management, 289, 112514, https://doi.org/10.1016/j.jenvman.2021.112514, 2021.

WMO (World Meteorological Organisation): Tropical cyclones. Retrieved May 06, 2020 from https://public.wmo.int/en/our-mandate/focus-areas/natural-hazards-and-disaster-risk-reduction/tropical-cyclones , 2020.

Wong, M. M. F., Fung, J. C. H., and Yeung, P. P. S.: High-resolution calculation of the urban vegetation fraction in the Pearl River Delta from the Sentinel-2 NDVI for urban climate model parameterization, Geoscience Letters, 6(1), 1-10, https://doi.org/10.1186/s40562-019-0132-4, 2019.

Xu, S., Zhu, X., Helmer, E. H., Tan, X., Tian, J., and Chen, X.: The damage of urban vegetation from super typhoon is associated with landscape factors: Evidence from Sentinel-2 imagery, International Journal of Applied Earth Observation and Geoinformation, 104, 102536, https://doi.org/10.1016/j.jag.2021.102536, 2021.

Yang, Q., Qin, Z., Li, W., and Xu, B.: Temporal and spatial variations of vegetation cover in Hulun Buir grassland of Inner Mongolia, China, Arid Land Research and Management, 26(4), 328-343, https://doi.org/10.1080/15324982.2012.709215, 2012.

Yang, Y., Erskine, P. D., Lechner, A. M., Mulligan, D., Zhang, S., and Wang, Z.: Detecting the dynamics of vegetation disturbance and recovery in surface mining area via Landsat imagery and LandTrendr algorithm, Journal of Cleaner Production, 178, 353-362, https://doi.org/10.1016/j.jclepro.2018.01.050, 2018.

Yin, J., Yin, Z., and Xu, S.: Composite risk assessment of typhoon-induced disaster for China's coastal area, Natural hazards, 69(3), 1423-1434, https://doi.org/10.1007/s11069-013-0755-2, 2013.

Yoon, W. S., Yoon, S. H., Moon, J. H., and Hong, J. S.: Topographic Variability during Typhoon Events in Udo Rhodoliths Beach, Jeju Island, South Korea, Ocean and Polar Research, 43(4), 307-320., 2021.

Yu, J. J., Kim, D., and Yoon, J.: A Study on the Short-term Morphological Beach Changes of Pado-ri Using UAS-based DEM: Focusing on before and after Typhoon Soulik, Journal

https://doi.org/10.5194/nhess-2022-253
Preprint. Discussion started: 9 November 2022

of the Association of Korean Geographers, 7(3), 303-317, 2018.

Yum, S. G., Wei, H. H., and Jang, S. H.: Estimation of the non-exceedance probability of extreme storm surges in South Korea using tidal-gauge data, Natural Hazards and Earth System Sciences, 21(8), 2611-2631, https://doi.org/10.5194/nhess-21-2611-2021, 2021.

Zhang, X., Wang, Y., Jiang, H., and Wang, X.: Remote-sensing assessment of forest damage by Typhoon Saomai and its related factors at landscape scale, International Journal of Remote Sensing, 34(21), 7874-7886, https://doi.org/10.1080/01431161.2013.827344, 2013.

Zhang, Y., Sun, Y., Hu, Z., Bian, S., Xiong, C., Liu, J., ... , and Zhang, W.: Increase in Suspended Sediment Contents by a Storm Surge in Southern Bohai Sea, China, Mathematical Problems in Engineering, 2022, https://doi.org/10.1155/2022/9585386, 2022.